Parcel Helicity in a Secondary-Flow Model

Robert Peter Davies-Jones [a]

[a] *Remote corner of a black hole*

D-J Research Papers, **2**.

June 2025

Corresponding author: Dr. Robert Davies-Jones, bobdj1066@yahoo.com

ABSTRACT

Theoretical formulas for the parcel helicity (dilatation times the scalar product of storm-relative wind and vorticity) and abnormality (helicity divided by speed squared) of fluid parcels were developed previously. In this paper, these quantities are computed in an analytical model of flow around and underneath a sphere. The model assumes a primary potential flow and deduces the secondary vorticity that develops when environmental vertical shear and stratification are included as secondary effects. The only source of error is the assumption that the streamlines are those of the primary flow. Because the secondary velocity is neglected, the general solution for helicity is a linear combination of three basic solutions. The first and second solutions are for the cases of neutral stratification with environmental vorticity that is either purely streamwise or purely crosswise. The third solution is for the case of environmental stratification without environmental vorticity.

Although the ultimate goal is to understand tornadogenesis and improve tornado forecasts and warnings, the analytical model has little relevance to tornadoes. The aim herein is to illustrate the generation and amplification of parcel helicity and abnormality in fluid flows. Plots of model results illustrate how curved flow turns environmental and baroclinically generated transverse vorticity streamwise to generate parcel helicity, and how the flow amplifies existing and baroclinically generated helicity through streamwise stretching of streamwise vorticity.

SIGNIFICANCE STATEMENT

The helicity of a parcel (scalar product of its vorticity and storm-relative wind) increases by two orders of magnitude during its passage from the environment to a tornado. An analytical model is used to illustrate how helicity is generated and amplified in fluid flows. Although the helicity gains in the model are modest, the model serves its purpose in explaining the basic physics of helicity amplification. Ensuing improved understanding of how supercell storms generate tornadoes should lead eventually to improved tornado forecasts and warnings.

Introduction

In Davies-Jones (2025a; hereafter DJ25), theoretical formulas for parcel helicity (dilatation times the scalar product of storm-relative velocity and vorticity) and abnormality (parcel helicity divided by windspeed squared) were developed, and it was shown that the helicity and abnormality of a parcel increases by two to three orders of magnitude and by an order of magnitude, respectively, during its passage from the environment to a tornado. In this paper, the Davies-Jones (2000) analytical model is used to demonstrate how helicity and abnormality is generated and amplified in fluid flows.

The analytical model assumes a steady state with a primary potential flow. Environmental vertical shear and stratification are introduced as secondary effects and the secondary vorticity is calculated. In this paper, we also compute the parcel helicity and abnormality. The assumption that the streamlines are those of the primary flow is the only source of error in the helicity and abnormality calculations. Because the secondary velocity is neglected, the general solution for helicity is a linear combination of three fundamental solutions, namely for (i) neutral stratification with streamwise environmental vorticity, (ii) neutral stratification with crosswise environmental vorticity, (iii) unstable environmental stratification with no environmental vorticity. These three cases illustrate how curved flow turns environmental and baroclinically generated transverse vorticity streamwise to generate parcel helicity, and how the flow amplifies existing and baroclinically generated helicity through streamwise stretching of streamwise vorticity.

Section 2 summarizes the formulas developed in DJ25. In section 3, the role of flow curvature in helicity generation is discussed in general terms. Section 4 presents helicity and abnormality fields generated by the analytical model for the three basic solutions.

2. Summary of formulas in D25

In this section, we list the relevant formulas from DJ25, adapted to steady Boussinesq isentropic flow in a horizontally uniform environment for easy reference. Since the flow is Boussinesq, $\alpha = \alpha_0$, and the **w** and vorticity vectors are identical. The potential vorticity of this flow is zero. The notation is the same as in DJ25.

The velocity formula is

$$\mathbf{v} = \nabla\phi + \chi\nabla Z \tag{2.1}$$

78 where

79 $$\phi = \Phi + q_0 s_0, \tag{2.2}$$

80 $$\chi = -\frac{dq_0}{dZ} s_0 - q_0 \frac{d\beta_0}{dZ} n_0 + c_p \frac{d\theta}{dZ} \Pi, \tag{2.3}$$

81 $$\Phi(\tau) = \int_{\tau'=\tau_0}^{\tau} \left[q^2(\tau') - q_0^2(Z) \right] d\tau' , \tag{2.4}$$

82 $$\Pi(\tau) = \int_{\tau'=\tau_0}^{\tau} [\pi(\tau') - \pi_0(Z)] d\tau' . \tag{2.5}$$

83 Since the flow is steady,

84 $$d\tau = ds_0/q_0 \tag{2.6}$$

85 in (2.4) and (2.5). By the curl of (2.1), the vorticity is

86 $$\boldsymbol{\omega} = \nabla\chi \times \nabla Z. \tag{2.7}$$

87 The vortex lines are the isopleths of χ. The parcel helicity

88 $$h \equiv \mathbf{v} \cdot \mathbf{w} = \nabla\phi \cdot \boldsymbol{\omega} = \nabla\phi \cdot \nabla\chi \times \nabla Z = \frac{\partial(\phi, \chi, Z)}{\partial(x, y, z)} \tag{2.8}$$

89 in terms of a Jacobian. The Lagrangian continuity equation for Boussinesq flow is

90 $$\nabla s_0 \cdot \nabla n_0 \times \nabla Z = \frac{\partial(s_0, n_0, Z)}{\partial(x, y, z)} = 1 \tag{2.9}$$

91 (Salmon 1998, p. 6). Hence, by properties of Jacobians,

92 $$h = \frac{\partial(\phi, \chi, Z)}{\partial(x, y, z)} \frac{\partial(x, y, z)}{\partial(s_0, n_0, Z)} = \frac{\partial(\phi, \chi, Z)}{\partial(s_0, n_0, Z)} \tag{2.10}$$

93 in (s_0, n_0, Z) coordinates. Introducing (2.3) and (2.9) into (2.10) results in

94 $$h = \frac{\partial\phi}{\partial s_0} \left(-q_0 \frac{d\beta_0}{dZ} + c_p \frac{d\theta}{dZ} \frac{\partial\Pi}{\partial n_0} \right) + \frac{\partial\phi}{\partial n_0} \left(\frac{dq_0}{dZ} - c_p \frac{d\theta}{dZ} \frac{\partial\Pi}{\partial s_0} \right). \tag{2.11}$$

95 Via differentiation of (2.4) and (2.5) with use of (2.6),

96 $$\frac{\partial\Pi}{\partial s_0} = \frac{\pi - \pi_0}{q_0}, \tag{2.12}$$

97 $$\frac{\partial\phi}{\partial s_0} = q_0 + \frac{\partial\Phi}{\partial s_0} = q_0 + \frac{q^2 - q_0^2}{q_0} = \frac{q^2}{q_0}. \tag{2.13}$$

98 Introducing (2.12) and (2.13) into (2.11) yields

99 $$h = -q^2 \frac{d\beta_0}{dZ} + \frac{\partial \phi}{\partial n_0}\frac{dq_0}{dZ} + \left(\frac{q^2}{q_0}\frac{\partial \Pi}{\partial n_0} - \frac{\partial \phi}{\partial n_0}\frac{\pi - \pi_0}{q_0}\right) c_p \frac{d\theta}{dZ}. \tag{2.14}$$

100 Hence, the abnormality of a parcel is

101 $$\lambda \equiv \frac{h}{q^2} = -\frac{d\beta_0}{dZ} + \frac{1}{q^2}\frac{\partial \phi}{\partial n_0}\frac{dq_0}{dZ} + \left(\frac{1}{q_0}\frac{\partial \Pi}{\partial n_0} - \frac{1}{q^2}\frac{\partial \phi}{\partial n_0}\frac{\pi - \pi_0}{q_0}\right) c_p \frac{d\theta}{dZ}. \tag{2.15}$$

102 An alternative expression for λ, derived in DJ25, is,

103 $$\lambda = -\frac{d\beta_0}{dZ} + \int_{-\infty}^{s} \frac{2\kappa \boldsymbol{\omega} \cdot \mathbf{n}}{q} ds' + \int_{-\infty}^{s} \frac{\mathbf{t} \cdot \nabla \pi \times c_p \nabla \theta}{q^2} ds' . \tag{2.16}$$

104 Since the barotropic terms in (2.15) and (2.16) must be equal, we obtain

105 $$\frac{\partial \phi}{\partial n_0} = \frac{q^2}{dq_0/dZ} \int_{-\infty}^{s} \frac{2\kappa \boldsymbol{\omega} \cdot \mathbf{n}}{q} ds' . \tag{2.17}$$

106 Clearly, $\partial\phi/\partial n_0$ depends on the parcel's history of flow curvature.

107 We also need the formula for the Bernoulli function B, which is constant on each material
108 surface of constant Z in a steady inviscid isentropic flow with a horizontally uniform
109 upstream environment. $B(Z)$ is the total parcel energy (the sum of specific kinetic energy,
110 $q^2/2$, specific enthalpy, c_pT, and specific potential energy, gz). Thus

111 $$B(Z) = q^2/2 + c_p\theta(Z)\pi + gz = \frac{q_0^2(Z)}{2} + c_p\theta(Z)\pi_0(Z) + gZ. \tag{2.18}$$

112 For reference in section 4, we partition χ in (2.3) according to

113 $$\chi = \chi_{\mathrm{BTIC}} + \chi_{\mathrm{BTIS}} + \chi_{\mathrm{BC}},$$

114 $$\chi_{\mathrm{BTIC}} = -\frac{dq_0}{dZ} s_0, \chi_{\mathrm{BTIS}} = -q_0 \frac{d\beta_0}{dZ} n_0, \chi_{\mathrm{BC}} = c_p \frac{d\theta}{dZ} \Pi. \tag{2.19}$$

115 Here and below, subscripts BTIC, BTIS and BC refer to the parts of a quantity that are
116 associated with imported crosswise vorticity, imported streamwise vorticity and baroclinic
117 vorticity, respectively.

118 Finally, note that the covariant basis vectors in the tangent plane of the Z-surface are

119 $$\mathbf{f}_1 = \frac{\partial \mathbf{x}}{\partial s_0} = \nabla n_0 \times \nabla Z, \mathbf{f}_2 = \frac{\partial \mathbf{x}}{\partial n_0} = \nabla \mathrm{Z} \times \nabla s_0. \tag{2.20}$$

3. The role of flow curvature

We now employ the helicity perspective to show when the curvature effect is significant in supercell dynamics. Using linear theory, DJ84 (see his eq. 23) showed that updraft helicity (the product of vertical velocity and vertical vorticity), when averaged across an updraft, is proportional to storm-relative environmental helicity. More simply, the updraft rotates cyclonically due to upward tilting of streamwise environmental vorticity. Environmental air flows around the outside of the rotating updraft and turns to the left due to the centripetal conservative pressure-gradient force associated with the low in the helical updraft. Inevitably, flow curvature affects the dynamics of a supercell, as discussed in Adlerman et al. (1999), Davies-Jones et. al. (2001), Davies-Jones (2017) and Davies-Jones (2022). Some simple schematics (Figs. 1-4) summarize the roles played by the curvature and baroclinic terms in (2.16) in producing parcel abnormality. We consider four extreme cases of steady flow.

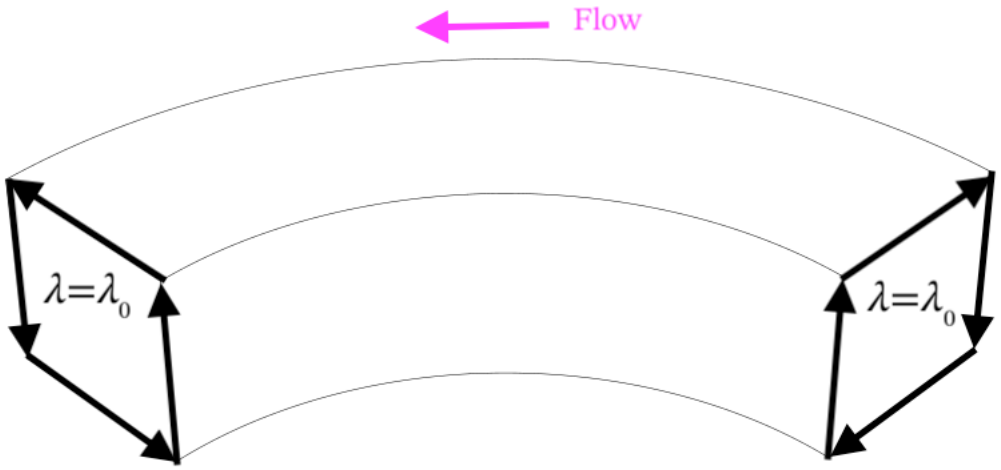

FIG. 1. Schematic of the constant abnormality λ_0 in a Beltrami flow. The thick black arrows indicate the secondary circulation. The thin black lines are streamlines. Here, streamline curvature has no effect on λ and parcel helicity varies in proportion to q^2.

The first case is a steady barotropic flow with purely streamwise vorticity. It is a Beltrami flow, which is inherently homentropic (Lilly 1982). Since the curvature factor (in

(2.16) acts on transverse vorticity and there is none in this case, the flow exits the bend with the same abnormality, λ_0, as it enters with (Fig. 1). Thus (2.16) reduces to

$$\lambda = \lambda_0 = -\frac{d\beta_0}{dZ}. \tag{3.1}$$

and $h = \lambda_0 q^2$ where the factor q^2 accounts for streamwise stretching of both the vortex tubes and stream tubes.

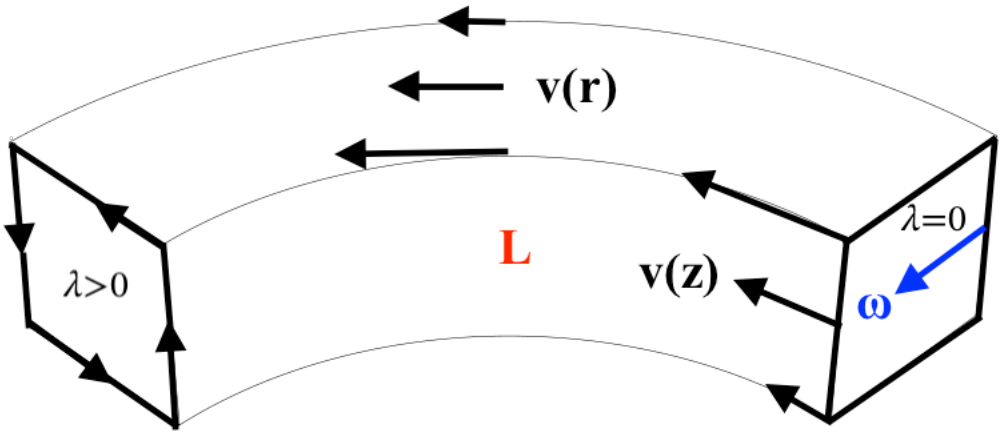

FIG. 2. 3D diagram of barotropic abnormality development around a left-hand bend (thin black lines). Black arrows on the inner bank of the bend entrance indicate the vertical profile **v**(z) of the environmental flow, which has positive speed shear and no helicity or abnormality. The blue arrow indicates the direction of the transverse vorticity entering the bend. The black arrows on the top face depict the lateral profile of downstream velocity, denoted by **v**(r), where r is distance from the bend's center of curvature. The red "L" indicates low pressure on the inside of the bend. High pressure on the outside of the bend is not shown. The black arrows and the annotation at the exit of the bend indicate the sense of the secondary transverse circulation and abnormality produced in the bend (adapted from Davies-Jones and Markowski 2021 and Davies-Jones 2022).

The other limiting barotropic case is the classic river-bend flow where the upstream vorticity is purely crosswise. The river of air in this context is proxy for a stream tube. In this case, the abnormality formulas (2.15) and (2.16) simplify to

$$\lambda = \frac{1}{q^2}\frac{\partial \Phi}{\partial n_0}\frac{dq_0}{dZ} = \int_{-\infty}^{s} \frac{2\kappa \mathbf{w}\cdot\mathbf{n}}{q} ds' . \tag{3.2}$$

where $\partial\Phi/\partial n_0$ is related to curvature through (2.17). This link is evident on physical grounds because a centripetal pressure-gradient force towards the center of curvature is needed to turn the flow. In a supercell, the pressure gradient is a result of low pressure in the mesocyclone and a mesohigh in the rain-cooled downdraft (e.g., MR14). It follows from (3.1) that

$$h \equiv \lambda q^2 = \frac{\partial \Phi}{\partial n_0}\frac{dq_0}{dZ}. \tag{3.3}$$

Thus, the airstream enters the bend with no helicity and exits with positive helicity (Fig. 2) [or negative helicity if the bend is right-handed]. On the mesoscale, a favored location for tornadoes is near the intersection of a dry line and front (a 'triple point'). Here, inflow into a supercell is curved leftward by the subsynoptic low at the triple point and its helicity is augmented by the riverbend effect if there is positive speed shear.

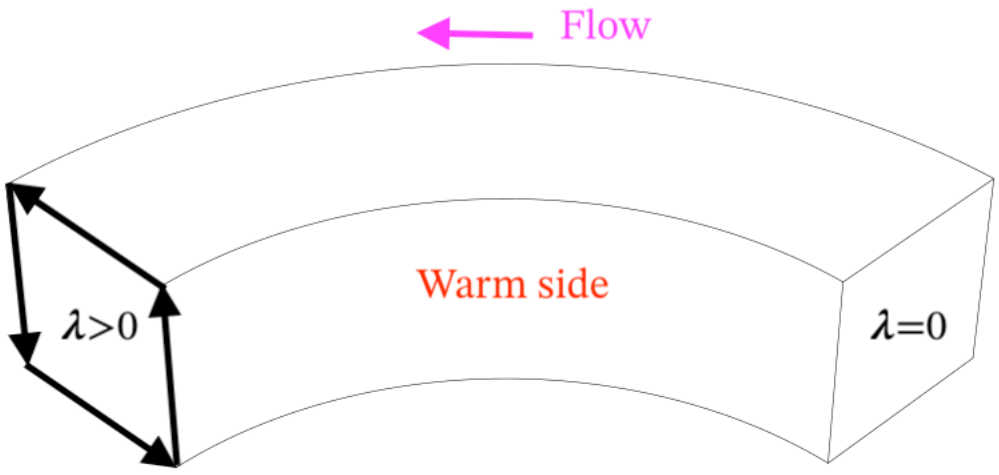

FIG. 3. Illustration of direct baroclinic generation of helicity and abnormality. The upstream flow is devoid of vorticity. The leftward buoyancy gradient generates the circulation and abnormality indicated on the downstream cross section of the stream tube. Flow curvature is irrelevant here.

To isolate baroclinic effects, we stipulate that the upstream environmental flow is irrotational. In this case, (2.14) reduces to

$$h = \left(\frac{q^2}{q_0}\frac{\partial \Pi}{\partial n_0} - \frac{\partial \Phi}{\partial n_0}\frac{\pi - \pi_0}{q_0}\right) c_p \frac{d\theta}{dZ}. \tag{3.4}$$

On an isentropic surface temperature is proportional to pressure. The first baroclinic limiting case is when the temperature or pressure gradient on each isentropic surface is across the flow and to the left of it. In this case, (3.4) implies that

$$\lambda = \frac{1}{q_0}\frac{\partial \Pi}{\partial n_0} c_p \frac{d\theta}{dZ} \tag{3.5}$$

In unstable stratification ($d\theta/dZ < 0$), the flow downstream obtains positive helicity and abnormality (Fig. 3) irrespective of flow curvature because the curl of the buoyancy force generates streamwise vorticity directly.

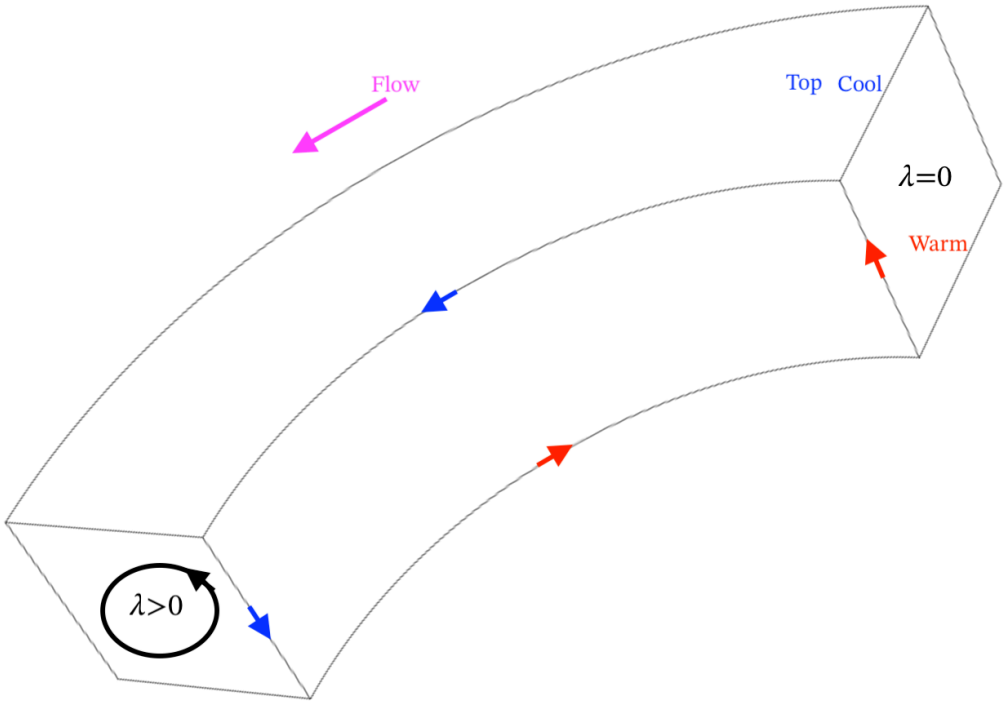

FIG. 4. Caricature of baroclinic abnormality generation in a downward tilting stream tube in an unstably stratified environment. The air on the top surface of the stream tube is potentially cooler than that on the bottom surface. The secondary circulation shown on a lateral face consists of cooler air sinking (blue arrows) and warmer air rising (red arrows). The bend effect acting on the associated transverse vorticity produces streamwise vorticity and abnormality as indicated on the downstream cross section of the stream tube.

198 In the other purely baroclinic limiting case, the temperature gradient on the isentropic
199 surface is downstream. In this case (3.4) simplifies to

200 $$h = \frac{\partial \Phi}{\partial n_0}\left(-\frac{\pi - \pi_0}{q_0} c_p \frac{d\theta}{dZ}\right). \tag{3.6}$$

201 As an example, consider the situation in Fig. 4 where unstably stratified isentropic flow is
202 subsiding and turning to the left. The factor in the parenthesis of (3.6) is accumulated
203 baroclinic vorticity. It is associated with the direct positive transverse circulation shown on
204 the side of the stream tube in Fig. 4. By (2.17) positive $\partial\Phi/\partial n_0$ is associated with positive
205 curvature. Thus, the river-bend effect generates positive helicity as the flow bends to the left.
206 In a supercell, this vorticity develops baroclinically in descending cyclonically revolving air
207 currents within the outer portion of the mesocyclone

208 We have shown that parcels gain helicity by turning left in the presence of positive speed
209 shear. One might expect that most trajectories in a mesocyclone are leftward. Paradoxically,
210 upward trajectories can turn anticyclonically in a cyclonically rotating supercell updraft.
211 Such trajectories exist because rising parcels encounter environmental winds that
212 progressively veer with height and act to turn them to the right, despite the vertical vorticity
213 being cyclonic (Lilly 1986). However, subsiding parcels experience consecutive
214 environmental winds that turn them leftward, i.e., the same direction as the rotation. So, we
215 can safely assume that most parcels in a twisting cyclonic downdraft do turn to the left.

216

217 **4. An illustrative flow example**

218 In this section we use a workable example to illustrate the theoretical fluid dynamics. We
219 considered using the MR14 toy model that mimics a supercell in a sheared environment by
220 utilizing a heat sink produces baroclinic vorticity at low levels. However, this flow is not
221 isentropic, so it does not exemplify the current theory. Instead, we look for an example where
222 the flow has zero PV, and the general shape of the steady-state isentropic surfaces determine
223 the temperature and curvature histories of individual parcels. Unfortunately, there are no
224 exact 3D analytical solutions with analytical trajectories that resemble a mesocyclone in a
225 horizontally uniform environment so instead we use a dissimilar analytical model (Davies-
226 Jones 2000, hereafter DJ00) to illustrate physical interpretation of the theoretical formulas in

DJ25. Unlike a tornadic storm, this model is incapable of obtaining large helicities. Nevertheless, it demonstrates the basic physics.

In the DJ00 model, the velocity **v** in (2.1) is partitioned into a primary irrotational wind $\mathbf{v}_{(1)}$ and a secondary rotational wind $\mathbf{v}_{(2)}$ where

$$\mathbf{v}_{(1)} = \nabla\phi, \mathbf{v}_{(2)} = \chi\nabla Z. \tag{4.1}$$

The model assumes that the wind is $\nabla\phi$ and the vorticity is $\nabla\chi\times\nabla Z$ so the model is strictly valid only when the secondary wind is small compared to the primary wind. Environmental vertical shear and stratification are introduced as small barotropic and baroclinic secondary effects that only affect the (secondary) vorticity. As shown in DJ25, the formulas for parcel helicity and abnormality are independent of $\mathbf{v}_{(2)}$. Computation of the parcel trajectories from $\mathbf{v}_{(1)}$ instead of from $\mathbf{v}_{(1)}+\mathbf{v}_{(2)}$ is only source of error in the computations of h and λ.

For the primary flow, we use incompressible westerly flow around a sphere of radius A centered at the origin (DJ00; DJ17). The potential temperature θ, environmental windspeed, q_0, and direction, β_0, are treated as constants in the irrotational primary flow. From eq. 7.1 of DJ00, the potential and velocity of this flow in Eulerian coordinates) with the x-axis aligned with the environmental wind in the Z_0-surface) are

$$\phi(x,y,z) = q_0 x\left[1+\frac{A^3}{(x^2+y^2+z^2)^{3/2}}\right], \qquad \mathbf{v} = \nabla\phi. \tag{4.2}$$

The primary flow satisfies continuity ($\nabla^2\phi = 0$) and the boundary conditions $\mathbf{v} = q_0\mathbf{i}$ at infinity and impermeability at the surface of the sphere.

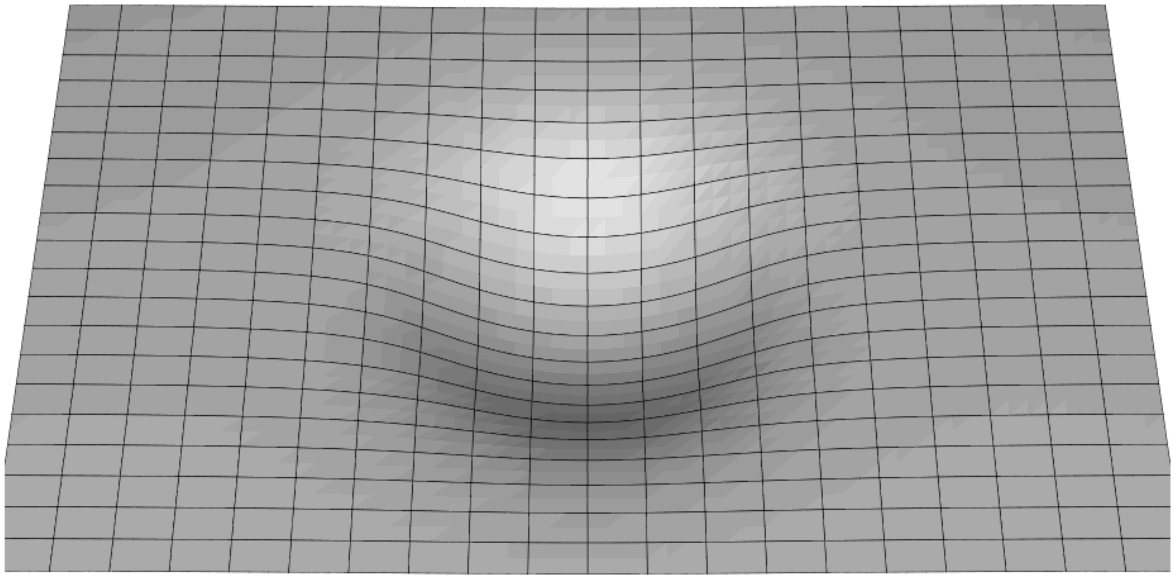

FIG. 5. Aerial perspective of the depression in the Z-surface. The $\mathbf{f}_1$ and $\mathbf{f}_2$ vectors are tangents to this surface, ∇Z is normal to it, and ∇s_0 and ∇n_0 are typically oblique to it.

We choose the particular material surface, $Z_0 = -A/2$, along which the flow passes around and under the obstacle. The topography of this surface is a circular depression (Fig. 5). On it we define a grid that is regularly spaced in x and y. For the primary flow, we choose A = 1000 m and $q_0 = 10$ m s^{-1}. The dilatation, α/α_0, on the surface varies by at most 5% from 1. This justifies use of the Boussinesq approximation. The heights $h(x, y)$ of the grid points on this surface are obtained by solving

$$h^2\left[1-\frac{A^3}{(x^2+y^2+h^2)^{3/2}}\right]=Z_0^2 \tag{4.3}$$

(DJ00 eq. 8.1). Since the flow is axisymmetric about the x-axis,

$$n_0(x,y)=\frac{y}{h}Z_0 \tag{4.4}$$

(DJ00 eq. 9.1). The wind and streamfunction on the surface are $\mathbf{v} = q_0\mathbf{f}_1$ and $\psi = q_0 n_0$.

We obtain the surface Lagrangian coordinates $s_0(x, y)$ and $n_0(x, y)$ via primary-wind trajectories calculated by Petterssen's method (Siebert 1993). Let t_0 be a long-ago time when all the parcels currently near the depression were in the far environment. To avoid large numbers in the computations, we redefine s_0 by adding the distance $q_0(t - t_0)$ that a parcel

would travel in the time interval $t - t_0$ if it moved with the constant environmental wind $q_0\mathbf{i}$. This procedure does not change ∇_{ZS0}. We check that the trajectories satisfy (4.4).

We obtain the pressure on the surface from constancy of the primary flow's Bernoulli function and the known height and wind speed on the surface. Thus,

$$c_p\theta(\pi - \pi_0) = g(Z_0 - h) + \left(q_0^2 - q^2\right)/2. \tag{4.5}$$

from (2.18). Apart from in severe windstorms, the KE term is small, so pressure on the surface typically decreases with height.

We compute cumulative quantities in the steady flow as in section 9 of DJ00. Because x increases monotonically along the streamlines, we can use the equation for a streamline to replace $d\tau$ by dx/u in the integrals in (2.4) and (2.5). Since we have found $h(x, y)$ and $n_0(x, y)$ from (4.3) and (4.4), we can evaluate any physical quantity as a function of x, n_0 and Z_0. Hence from (2.4), Φ can be expressed as

$$\Phi(x, n_0, Z_0) = \int_{x'=-\infty}^{x} \frac{q^2 - q_0^2}{u}\, dx' . \tag{4.6}$$

where the integrand is evaluated at points on the (n_0, Z_0)-streamline. Similarly, by performing the Lagrangian integral of (4.5), we obtain

$$c_p\theta\Pi(x, n_0, Z_0) = g\int_{-\infty}^{x} \frac{Z_0 - h}{u}\, dx' + \frac{1}{2}\int_{-\infty}^{x} \frac{q_0^2 - q^2}{u}\, dx' . \tag{4.7}$$

We also need formulas for computing the quantities $\partial\varphi/\partial s_0$ and $\partial\varphi/\partial n_0$ where φ is a generic scalar. We get these as follows. By the chain rule

$$\begin{bmatrix} \partial\varphi/\partial x \\ \partial\varphi/\partial y \end{bmatrix} = \begin{bmatrix} \partial s_0/\partial x & \partial n_0/\partial x \\ \partial s_0/\partial y & \partial n_0/\partial y \end{bmatrix} \begin{bmatrix} \partial\varphi/\partial s_0 \\ \partial\varphi/\partial n_0 \end{bmatrix}. \tag{4.8}$$

By matrix inversion,

$$\begin{bmatrix} \partial\varphi/\partial s_0 \\ \partial\varphi/\partial n_0 \end{bmatrix} = \frac{1}{\partial(s_0, n_0)/\partial(x, y)} \begin{bmatrix} \partial n_0/\partial y & -\partial n_0/\partial x \\ -\partial s_0/\partial y & \partial s_0/\partial x \end{bmatrix} \begin{bmatrix} \partial\varphi/\partial x \\ \partial\varphi/\partial y \end{bmatrix}. \tag{4.9}$$

Thus

$$\frac{\partial\varphi}{\partial s_0} = \frac{\partial(\varphi, n_0)/\partial(x, y)}{\partial(s_0, n_0)/\partial(x, y)}, \tag{4.10}$$

$$\frac{\partial\varphi}{\partial n_0} = \frac{\partial(s_0, \varphi)/\partial(x, y)}{\partial(s_0, n_0)/\partial(x, y)}. \tag{4.11}$$

All the above quantities are determined just by the primary flow, which is common to all cases.

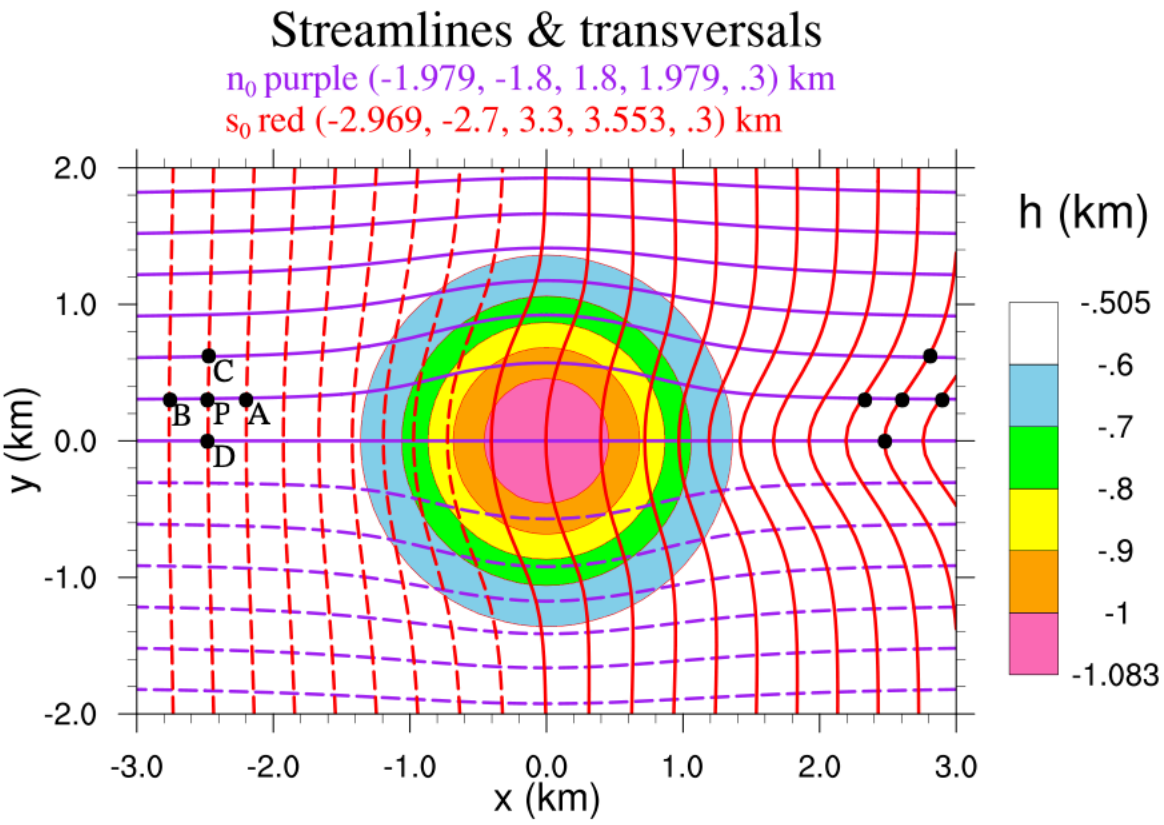

FIG. 6. The contours of n_0 (purple) and s_0 (red) within the surface $Z_0 = -500$ m for $A = 1000$ m, $q_0 = 10$ m s^{-1}. This diagram applies to all the cases. The environmental wind is from $x = -\infty$. The streamfunction and vortex-line functions are $\psi = q_0 n_0$, $\chi_{\mathrm{BTIC}} \equiv -s_0 dq_0/dZ$ and $\chi_{\mathrm{BTIS}} \equiv -n_0 q_0 d\beta_0/dZ$, so the purple contours are streamlines and vortex lines of imported streamwise vorticity, and the red contours are transversals (material lines that far upstream are crosswise to the wind) and vortex lines of imported crosswise vorticity. In this and subsequent figures, the parentheses enclose the minimum value of a field, the minimum contour value, the maximum contour value, the maximum value, and the contour interval, respectively. Negative contours are dashed. The colored filled contours in this figure and figures 8-14 are the height contours of the surface with contour levels supplied in the label bar at right. The black dots, •, define a tiny fluid cross (exaggerated for illustrative purposes) with arms APB and CPD. The fluid cross is shown when it is upstream and downstream of the obstacle. The flow is steady so parcels travel along their streamlines. PA and PC are the vectors $\mathbf{f}_1$ and $\mathbf{f}_2$ attached to parcel P.

The Z-surface at its nadir is only 83 meters lower than the bottom of the sphere whereas its height far upstream is 500 m above the lowest point of the sphere (Fig. 6). The purple lines (n_0 = const.) and red lines (s_0 = const.) in Fig. 6 are streamlines and transversals

(material lines that far upstream are transverse to the flow) of the primary flow. Since parcel trajectories on the right side are mirror images (reflection in the x-axis) of those on the left, we will generally describe just the left side ($y > 0$) of the flow. Left-side parcels approaching the depression initially slow and turn left. They then accelerate and turn to the right. They reach maximum speed as they cross the y-axis. The downstream portion of the trajectory is a mirror image (reflection in the y-axis) of the upstream part. Because of upstream flow deceleration and divergence, the transversals are held back and turn streamwise on the left side and antistreamwise on the right side (red lines in Fig. 6). This general shape is maintained downstream (Fig. 6).

Since barotropic vorticity is frozen in the fluid, we aid physical interpretation by considering a tiny fluid cross attached to a parcel P within the flow on the Z-surface (Dahl et al. 2014). The cross is shown greatly enlarged in Fig. 6. It starts out on the Z-surface in the environment with two horizontal orthogonal arms (as in fig. 5.15 in Davies-Jones et al 2001). Far upstream one arm APB is streamwise with parcels A and B a tiny distance Δ downstream and upstream from P when the cross is far upstream. The other arm CPD is initially perpendicular to AB with C and D distance Δ to the right and left of P. The vectors $\overrightarrow{\mathrm{PA}}/\Delta$ and $\overrightarrow{\mathrm{PD}}/\Delta$ are the covariant basis vectors $\mathbf{f}_1$ and $\mathbf{f}_2$. These are tangent to the streamlines and transversals, respectively. As the fluid cross travels downstream in the Z-surface, the streamwise arm remains streamwise as its parcels are tied to a streamline and the transversal arm turns relative to the streamwise arm. The wind vector $\mathbf{v} = q_0\mathbf{f}_1$. Due to mass conservation, the area of the parallelogram defined by $\mathbf{f}_1$ and $\mathbf{f}_2$ times the spacing of the Z-surfaces is equal to the dilatation (which is 1 in our Boussinesq flow).

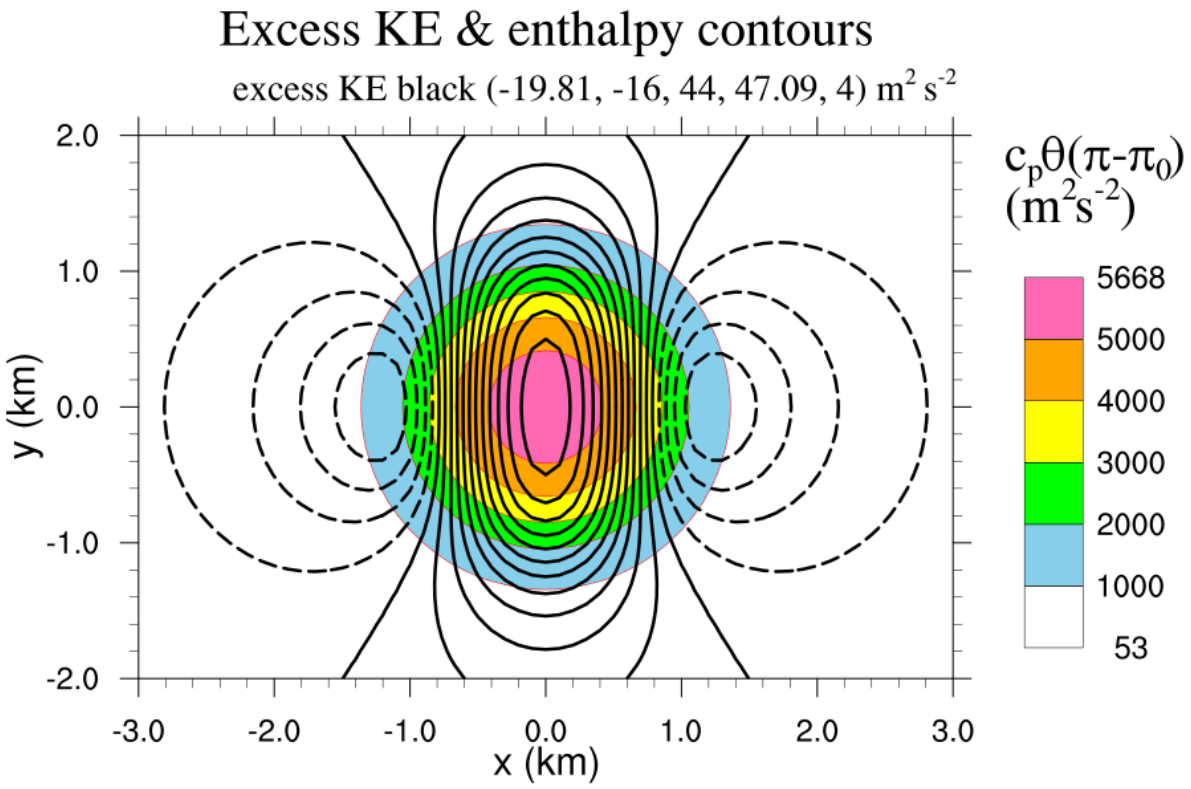

FIG.7. Contours of excess KE (black) and excess enthalpy (filled) in the primary flow on the Z_0-surface. The excesses are relative to values far upstream on the Z_0-surface.

Contours of excess KE are shown in Fig. 7. Parcels initially lose KE in divergent flow as they approach the depression, then gain KE as they pass through it before losing KE again in divergent flow downstream. Owing to flow constriction and mass conservation, the Z-surfaces are packed closer together immediately underneath the sphere. Consequently, the maximum speed of 14 m s^{-1} occurs on the Z_0-surface at its nadir. Since pressure typically decreases with elevation, the excess pressure on the Z_0-surface, $\pi - \pi_0$, is positive with a maximum at the origin (Fig. 7). Since θ is constant on the surface, the excess enthalpy, $c_p\theta(\pi-\pi_0)$, is also positive and centered on the origin.

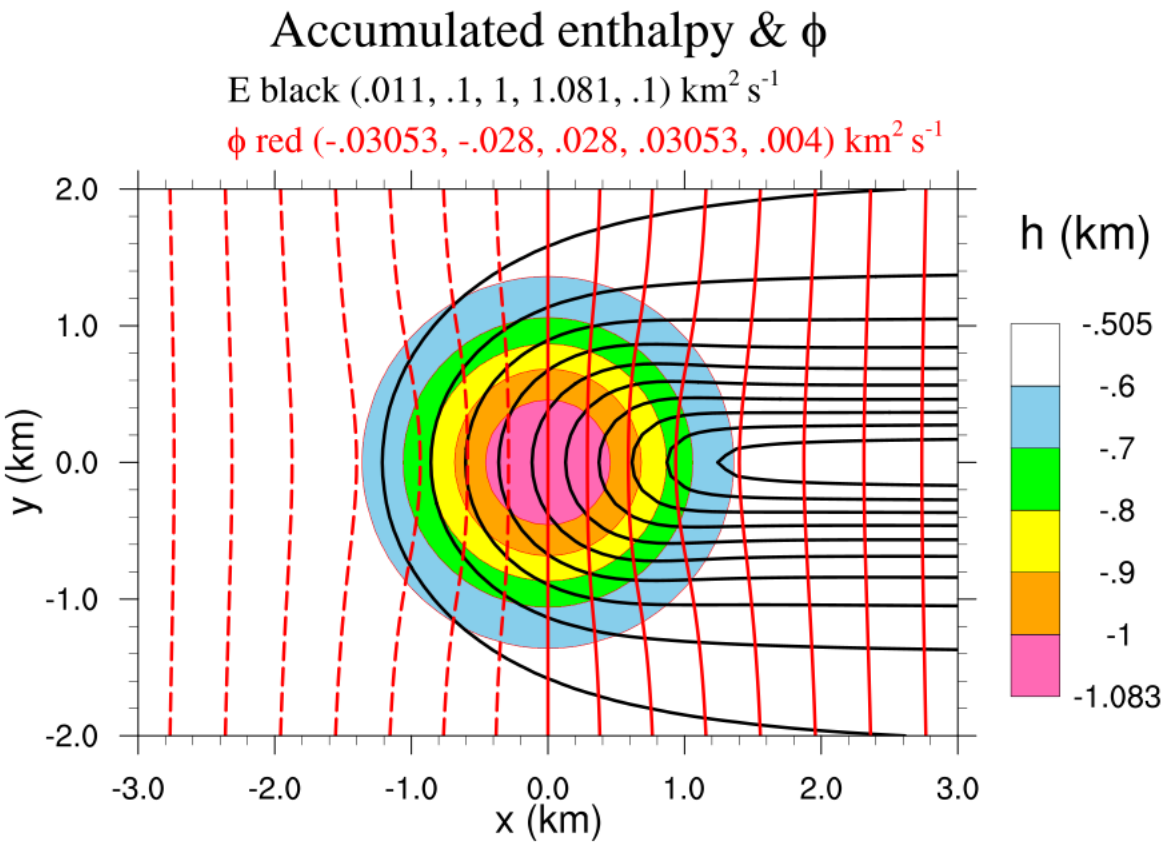

FIG. 8. The cumulative excess enthalpy field E (black) and contours of the velocity potential ϕ on the Z_0-surface (red) for the primary flow. The contours of Π are coincident with those of E.

The lines of equal potential ϕ are shown in red in Fig. 8. The wind is normal to these lines with windspeed inversely proportional to their spacing. The black lines are contours if cumulative excess enthalpy. Given the excess enthalpy field depicted in Fig. 7, the cumulative excess enthalpy, $E \equiv c_p \theta \Pi$, increases downstream and decreases laterally with distance from the centerline $y = 0$. Consequently, the contours of both E and Π are hairpins with arms extending downstream.

Environmental vertical shear and stratification are introduced as barotropic and baroclinic secondary effects. The secondary vorticity is computed from (2.7) and (2.3). For the secondary flow, we consider three extreme cases:

1. Beltrami flow ($-q_0 d\beta_0/dZ = 10^{-2}$ s^{-1}, $dq_0/dZ = d\theta/dZ = 0$),
2. Barotropic flow with only crosswise environmental vorticity ($dq_0/dZ = 10^{-2}$ s^{-1}, $d\beta_0/dZ = d\theta/dZ = 0$),

3. Purely baroclinic flow [$d\beta_0/dZ = dq_0/dZ = 0$, $\theta = 300$ K, $d\ln\theta/dZ = -10^{-5}$ m^{-1} as in Kuo (1966)].

Because the secondary velocity is neglected, more general cases are just linear combinations of these three cases. In cases 1 and 2, the vortex lines are frozen into the fluid.

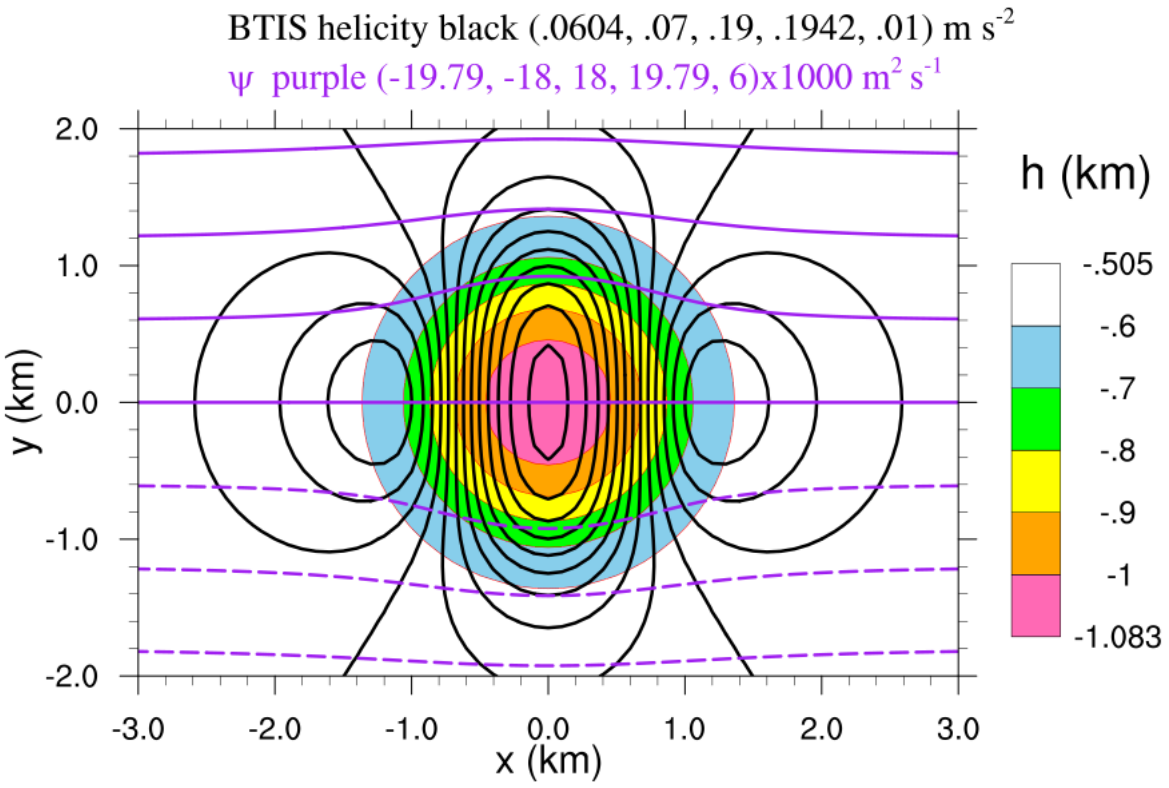

FIG. 9. The parcel-helicity field $\boldsymbol{\omega}_{BTIS}\bullet\mathbf{v}$ (black contours) for the Beltrami case 1 (purely streamwise vorticity). This field is simply $-q^2 d\beta_0/dZ$ where $-d\beta_0/dZ$, the abnormality, is constant (=1 km^{-1} here). Contours of ψ (purple) provide some streamlines.

We now describe the secondary vorticity, abnormality and parcel helicity in the three cases. In case 1, $\boldsymbol{\omega} = -q_0 d\beta_0/dZ\,\mathbf{f}_1$ so the material vector PA in Fig. 6 is proportional to the purely streamwise vorticity. The vortex lines, given by $\chi_{BTIS} \equiv -(q_0 d\beta_0/dZ)n_0 = $ const., are frozen to the streamlines and stretch with the flow. There is no vertical vorticity at the nadir of the trajectories ($x = 0$). From (3.1), the abnormality $\lambda_{BTIS} = -d\beta_0/dZ$, is constant (= 1 rad km^{-1}) and the parcel helicity is $-q^2 d\beta_0/dZ$. Consequently, the parcel helicity associated with imported streamwise vorticity is greatest at the sides and least immediately upstream and

379 downstream of the sphere (Fig. 9). Increasing helicity of a parcel in this case is simply due to
380 increase in its windspeed and to related stretching of its streamwise vorticity.

381

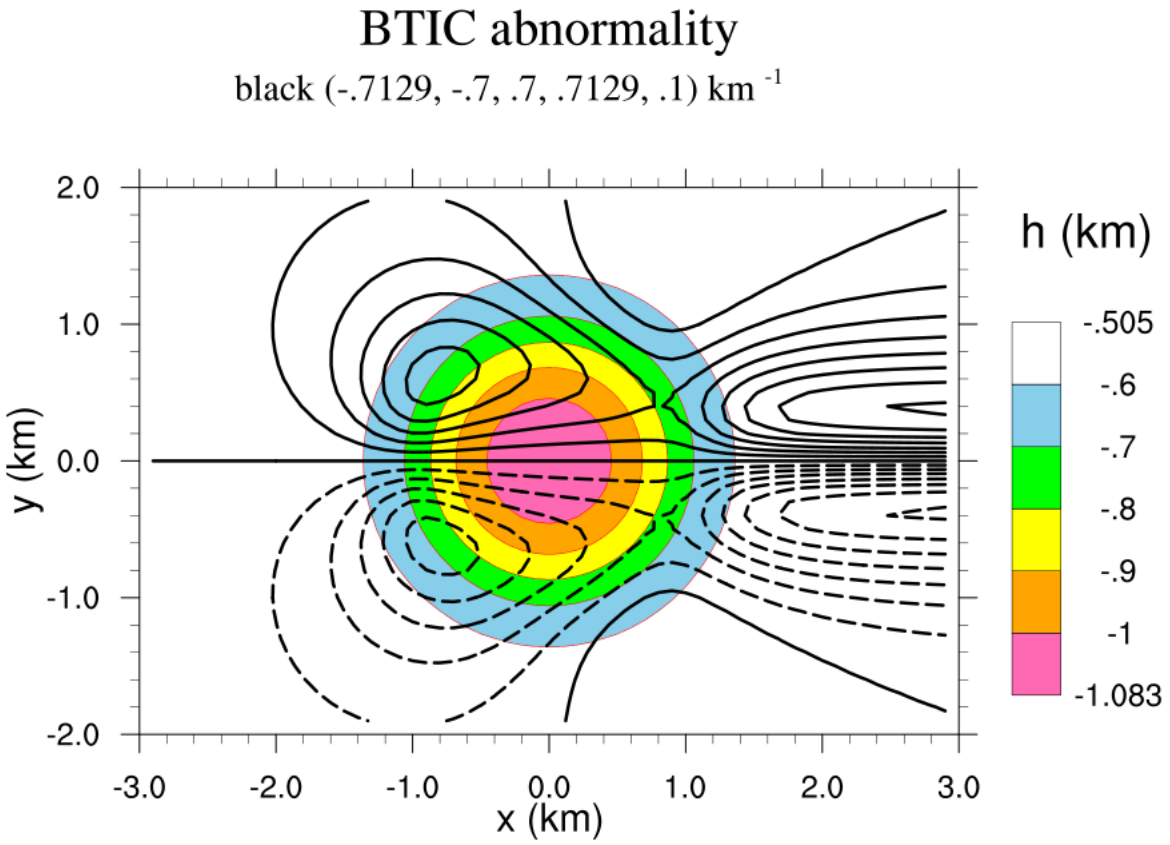

382

383 FIG. 10. The abnormality associated with barotropic imported crosswise vorticity (case 2).

384

385 In case 2, the environmental vorticity is purely crosswise. The barotropic vorticity is
386 frozen to the arm DPC of the fluid cross and is equal to the environmental crosswise
387 vorticity, dq_0/dZ, times $\mathbf{f}_2$. Streamwise vorticity is generated as DPC turns scissor-like
388 towards BPA. Because D and C lie on different streamlines, DC can become greatly
389 elongated as it turns towards BA. The vortex lines are the contours of $\chi_{\text{BTIC}} \equiv -(dq_0/dZ)s_0 =$
390 const. so the red contours in Fig. 6 are the vortex lines of imported crosswise vorticity as well
391 as the transversals. As evident from the transversals in Fig. 6, the vortex lines are directed
392 across the flow from right to left. They are turned partly streamwise on the left side of the
393 flow. At the nadirs of the left-sided trajectories ($x = 0$, $y > 0$), the vortex lines are directed
394 upslope so the vertical vorticity is positive there. From (2.16), the parcel abnormality arising
395 from imported crosswise vorticity is

$$\lambda_{\mathrm{BTIC}} = \int_{-\infty}^{s} 2\kappa\boldsymbol{\omega}\cdot\mathbf{n}\frac{ds'}{q}, \tag{4.12}$$

so λ increases along a streamline where it curves to the left and decreases where it curves to the right (Fig. 10). Because the left-side parcels initially turn to the left, there is a maximum of λ in the left rear quadrant ($x < 0$, $y > 0$) of the depression due to the river-bend effect (Fig. 10). The parcels then turn to the right as they flow around the obstacle, so λ diminishes for a while, even becoming negative for parcels moving along the outer streamlines. Further downstream, the parcels turn leftward once again, and λ increases. The maximum BTIC abnormality (> 0.7 m^{-1}) is downstream of the depression.

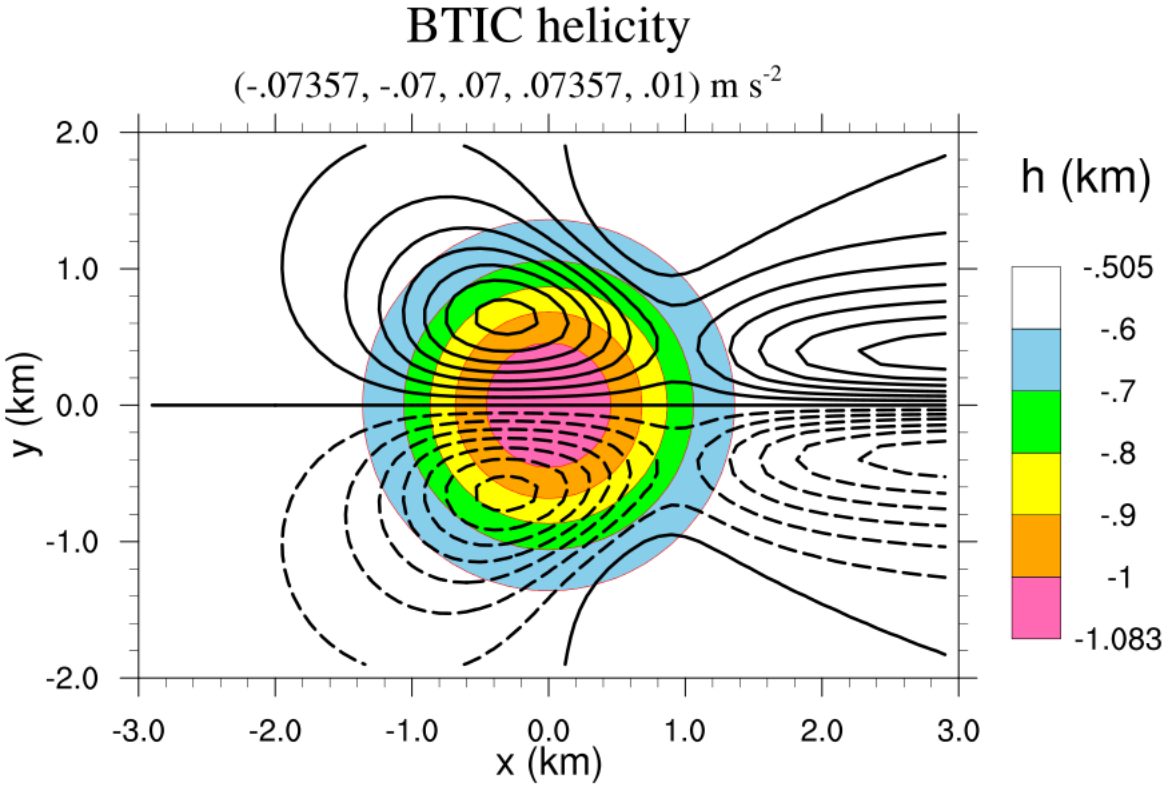

FIG. 11. The contours of helicity in case 2. This helicity is associated with imported crosswise vorticity and is equal to $(dq_0/dZ)\partial\phi/\partial n_0$ from (2.14) where $dq_0/dZ = 10^{-2}$ s^{-1} here. There is no helicity infinitely far upstream.

The barotropic helicity field (Fig. 11) is quite similar since $h = q^2\lambda$ as always. There is nonzero helicity at downstream infinity. Left-sided parcels nearest the centerline have the

shortest dwell times in the right-hand bend and always have positive helicity. Slower moving parcels to their left can have negative helicity for a while due to their spending a long time turning right.

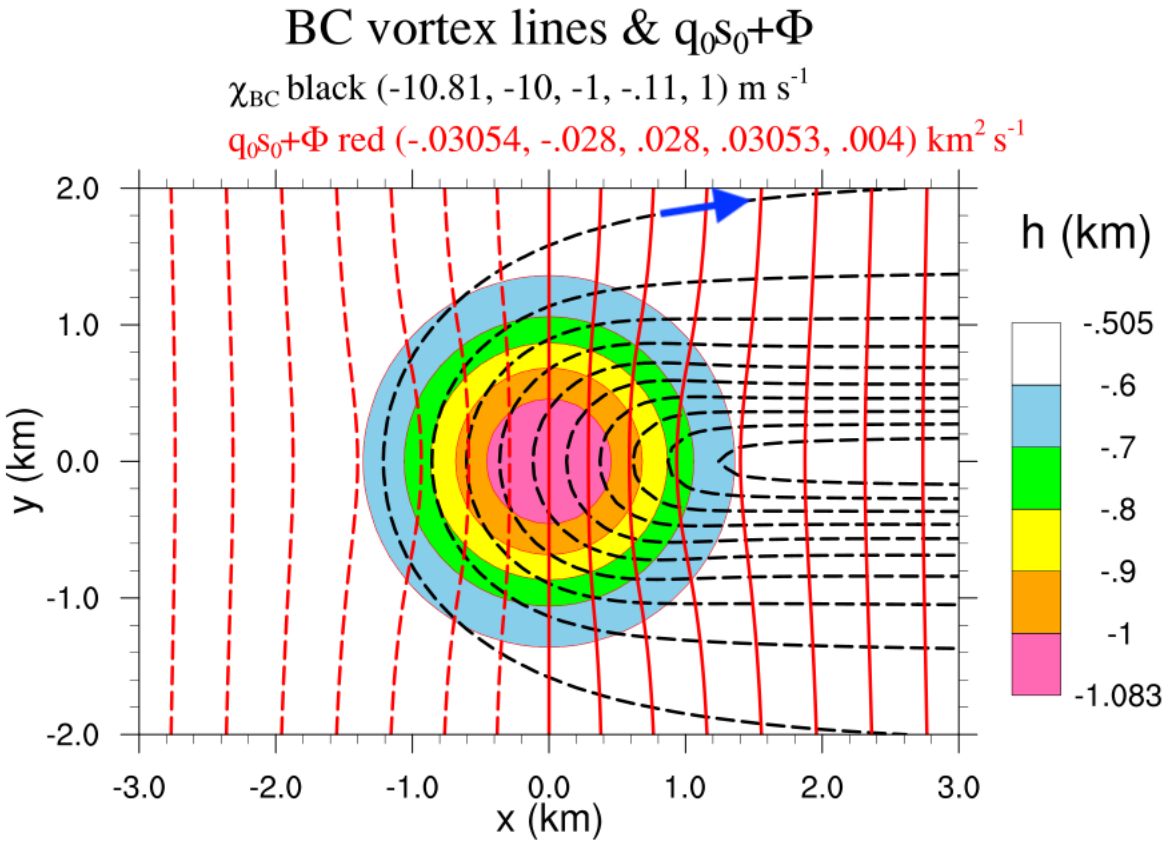

FIG. 12. The contours of $q_0s_0 + \Phi$ (red) and $\chi_{BC} \equiv (c_p d\theta/dZ)\Pi$ (black) in case 3. The $q_0s_0 + \Phi$ field is determined solely by the primary flow and is the same as the ϕ field (c.f. Fig. 8). The contours of χ_{BC} are proportional to those of cumulative excess enthalpy in Fig. 8. They are the baroclinic vortex lines. The blue arrow on one of the vortex lines indicates the direction of the vorticity.

From (2.19), the vortex lines in case 3 are the contours of $\chi_{BC} \equiv (c_p d\theta/dZ)\Pi$ = const. The stratification is unstable so $d\theta/dZ$ is negative. Hence, the χ_{BC} is similar to the Π field shown in Fig. 8, but with a change of sign. Alternatively, the vortex lines are coincident with the isopleths of cumulative temperature. Consequently, as deduced by DJ00, the vortex lines are hairpins in the Z-surface with arms extending to downstream infinity (Fig. 12). The baroclinic vortex lines have this shape as a result of generation of baroclinic vorticity in the depression and subsequent downstream advection. By (2.7), (2.19) and the above definition of E,

$$\omega_{\mathrm{BC}} = \nabla\chi_{\mathrm{BC}} \times \nabla Z = \frac{1}{\theta}\frac{d\theta}{dZ}\nabla E \times \nabla Z. \tag{4.13}$$

Since $\partial E/\partial y < 0$ on the left side of the flow (Fig. 8), the vorticity far downstream is streamwise on the left side. At the nadirs of the left-sided trajectories, the vortex lines are directed upslope, indicating positive vertical vorticity there (DJ00).

The red curves in Fig. 12 are the contours of $q_0 s_0 + \Phi$ in the primary flow. Comparison with Fig. 8 confirms that, on the Z_0-surface, the $q_0 s_0 + \Phi$ field is identical to the ϕ-field.

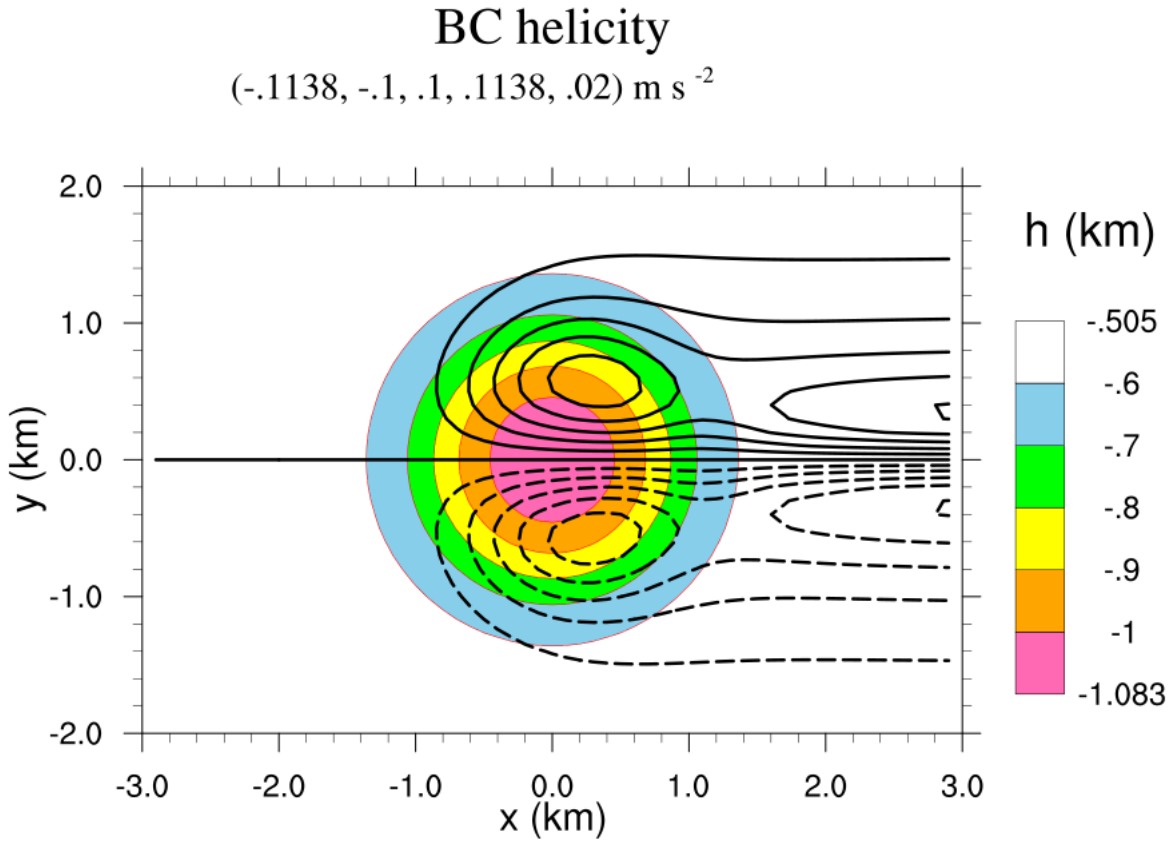

FIG. 13. The contours of baroclinic helicity in case 3.

From (2.11) and the definition of cumulative excess enthalpy ($E \equiv c_p\theta\Pi$), the parcel baroclinic helicity is

$$h = \frac{\partial\phi}{\partial s_0}\frac{\partial \mathrm{E}}{\partial n_0}\frac{1}{\theta}\frac{d\theta}{dZ} - \frac{\partial\phi}{\partial n_0}\frac{\partial \mathrm{E}}{\partial s_0}\frac{1}{\theta}\frac{d\theta}{dZ}. \tag{4.14}$$

Contours of this field and the two individual terms in (4.14) are shown in Figs. 13-15. Consistent with the baroclinic vortex lines depicted in Fig. 12, the baroclinic helicity field is

antisymmetric about the y-axis with positive values on the left side of the flow (Fig. 13). It has a maximum on the left front side of the depression.

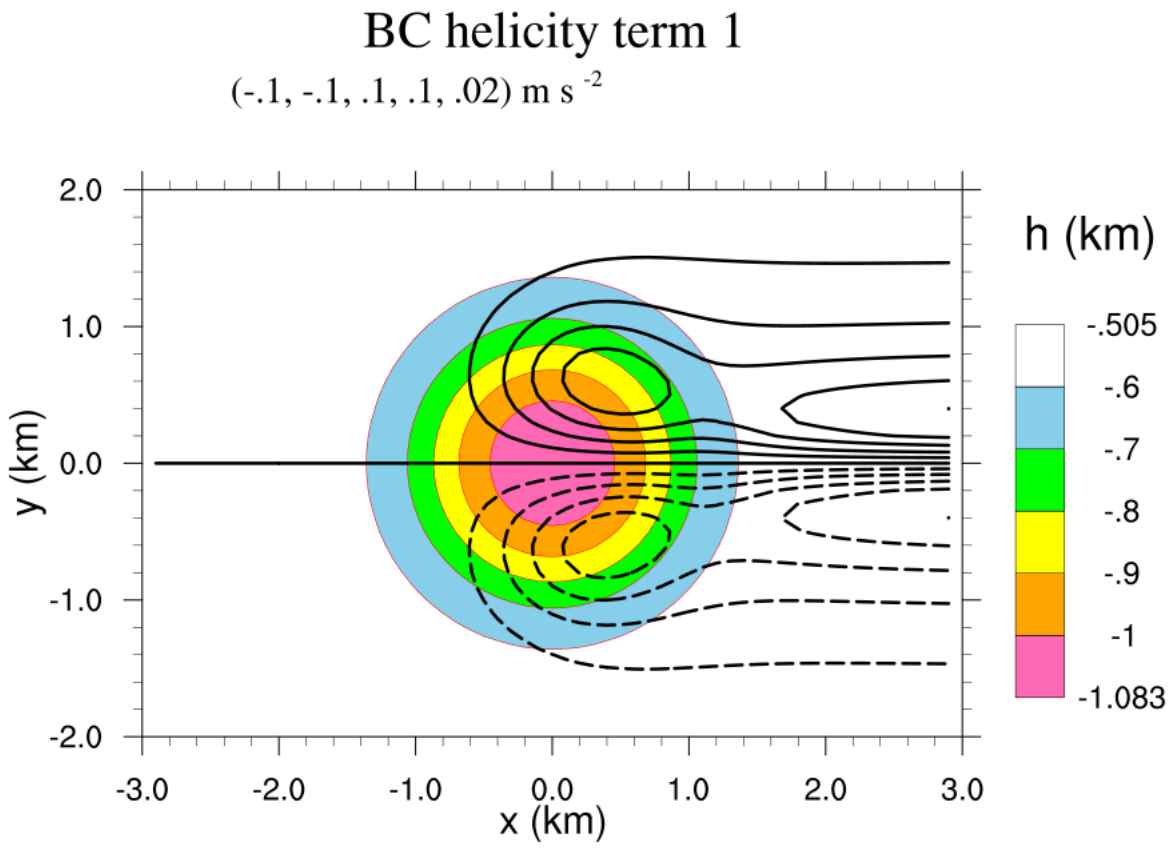

Fig. 14. Contours of the part of baroclinic helicity associated with transverse temperature gradients.

As described in section 3, the baroclinic helicity consists of parts associated with crosswise and streamwise temperature gradients. Respectively, these are the first and second terms on the right of (4.14). Because the enstrophy on the isentropic surface decreases with distance from the centerline of the flow, the cumulative enstrophy of parcel C in the stencil shown in Fig. 6 is less than that of parcel D. Hence $\partial E/\partial n_0 < 0$ on the left side of the flow. By similar reasoning, $\partial E/\partial n_0 > 0$ on the right side. Since ϕ increases downstream (Fig. 8), ϕ of parcel A is greater than that of parcel B. Consequently, $\partial\phi/\partial s_0 > 0$. Hence, the first term is positive on the left side of the flow and negative on the right side when the stratification is unstable ($d\theta/dZ < 0$).

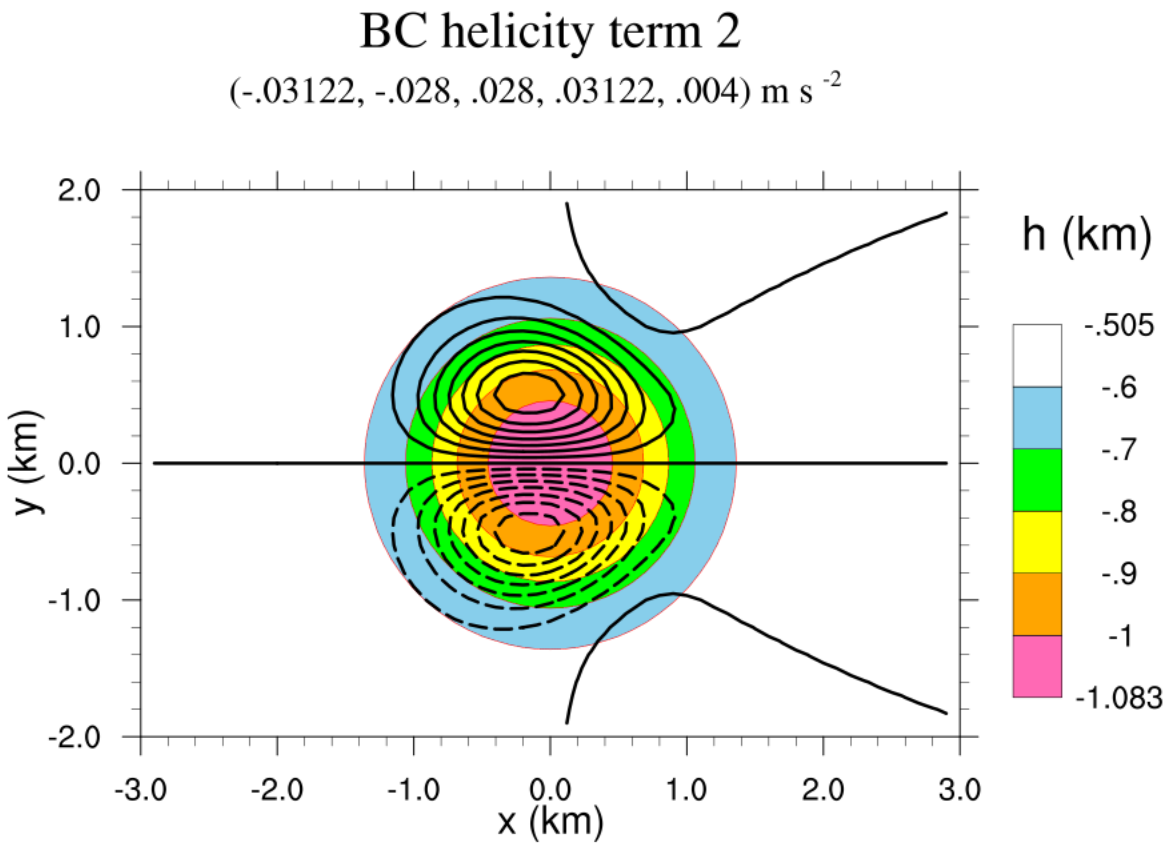

Fig. 15. Contours of the part of baroclinic helicity associated with streamwise temperature gradients.

For the chosen primary flow, the second term (Fig. 15) is much smaller than the first term. We can explain its dominant features as follows. Because parcel A is more advanced than B (Fig. 6) and cumulative enstrophy E increases downstream, $\partial E/\partial s_0 > 0$. At x =0, there is no transverse gradient of ϕ (Fig. 8). However, parcel C is further downstream than parcel D (Fig, 6). Since ϕ increases downstream (Fig. 8) and parcel C has the larger n_0 (Fig. 6), $\partial\phi/\partial n_0 > 0$ on the left side of the flow at x =0. Thus, the second term is mainly positive on the left side of the flow when $d\theta/dZ < 0$. Conversely, it is mainly negative on the right side.

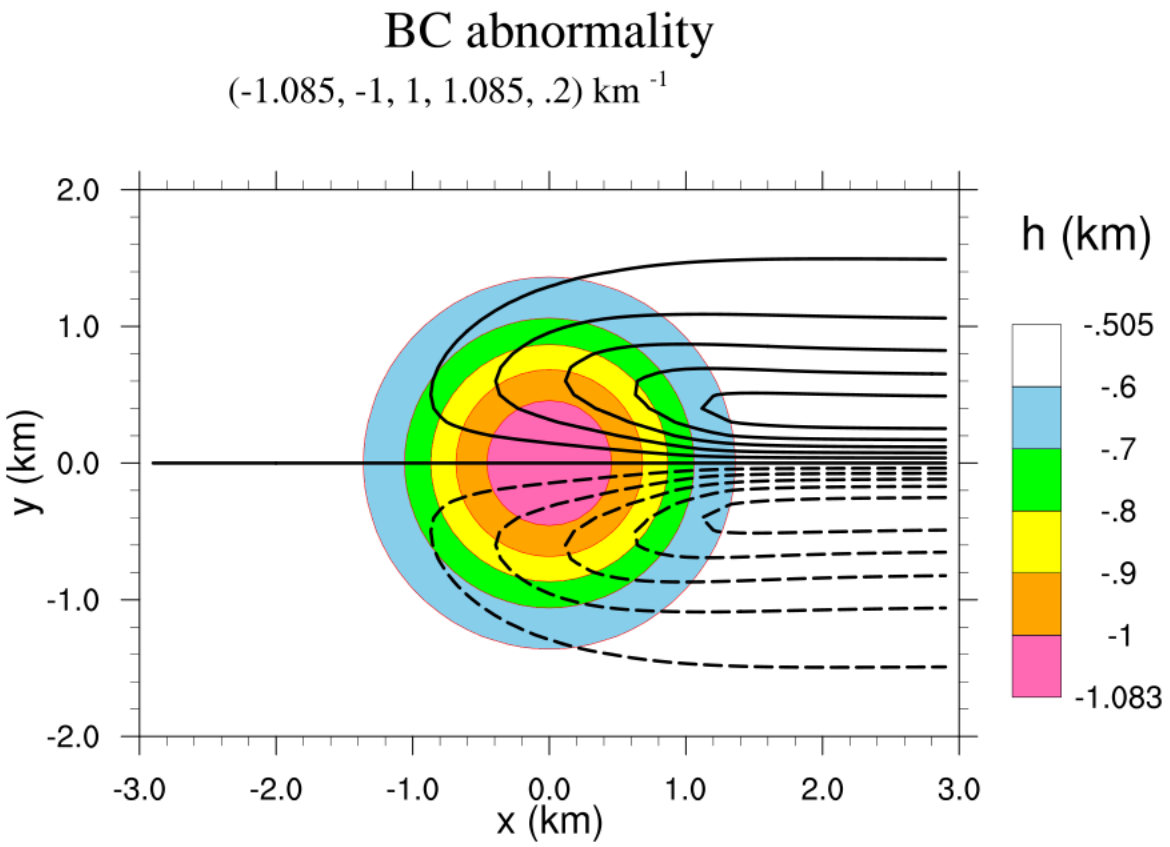

FIG. 16. The abnormality in case 3.

Since $\lambda = h/q^2$, the abnormality field is similarly antisymmetric about the y-axis with positive values on the left side (Fig. 16). Its magnitude is less than 1.09 km^{-1}. Parcels retain substantial baroclinic abnormality downstream.

5. Conclusions

We have utilized the DJ00 steady-state secondary-vorticity model to illustrate properties of parcel helicity (essentially the scalar product of a parcel's velocity and vorticity) and abnormality (parcel helicity divided by windspeed squared) that were deduced theoretically in DJ25. Because we neglect the secondary wind, there are three main cases to consider. All other cases are linear combinations of these cases.

In the first case, the flow is barotropic with purely streamwise vorticity. The abnormality is constant everywhere and the helicity simply varies with the square of the windspeed. The second case concerns barotropic flow with vorticity that far upstream is purely crosswise.

Environmental helicity is absent. When the environmental speed shear is positive, parcels gain helicity when they turn to the left and lose it when they turn to the right. In the third case, the flow is isentropic without environmental vorticity. Vorticity is generated baroclinically along the isotherms and swept downstream. The resulting vortex lines are hairpins coincident with the isopleths of cumulative temperature. This configuration associates with positive helicity on the left side and negative helicity on the right side of the flow when the thermal stratification is unstable.

The analytical DJ00 model fails to generate large increases in λ because parcels do not spend much time in (a) baroclinic zones that enable them to accumulate streamwise baroclinic vorticity, (b) in streamwise pressure gradients during descent, and (c) in long left-hand bends where any positive transverse vorticity that they possess is turned nearly streamwise and stretched. Better examples for significant generation of parcel helicity and abnormality are flow around a left-hand river bend where upstream crosswise vorticity (in the form of positive speed shear) is turned streamwise (Shapiro 1972; Scorer 1997) and the DJ08 axisymmetric tornadogenesis model. The development of large parcel helicities and abnormalities in the latter is investigated in Davies-Jones (2025b).

Acknowledgments. None.

Data Availability Statement. No datasets were generated or analyzed during the present study.

REFERENCES

Adlerman, E. J., K. K. Droegemeier, and R. Davies-Jones, 1999: A numerical simulation of cyclic mesocyclogenesis. *J. Atmos. Sci.,* **56,** 2045-2069.

Dahl, J. M. L., M. D. Parker, and L. J. Wicker, 2014: Imported and storm-generated near-ground vertical vorticity in a simulated supercell. *J. Atmos. Sci.*., **71**, 3027-3051.

Davies-Jones, R. P., 2000: A Lagrangian model for baroclinic genesis of mesoscale vortices. Part I: Theory. *J. Atmos. Sci*., **57**, 715–736.

517 Davies-Jones, R. P., 2017: Roles of streamwise and transverse partial-vorticity components in
518 steady inviscid isentropic supercell-like flows. *J Atmos. Sci*., **74**, 3021-3041.

519 Davies-Jones, R. P., 2022: Theory of parcel vorticity evolution in supercell-like flows. *J*
520 *Atmos. Sci*., **79**, 1253-1270.

521 Davies-Jones, R. P., 2025a: Theory of parcel helicity in supercell-like flows. *D-J Retirement*
522 *Papers*, **1**.

523 Davies-Jones, R. P., 2025b: Parcel helicity in an axisymmetric model of tornadogenesis. *D-J*
524 *Retirement Papers*, **3**.

525 Davies-Jones, R. P., and P. M. Markowski, 2021: Circulation around a constrained curve: An
526 alternative analysis tool for diagnosing the origins of tornado rotation in numerical
527 supercell simulations. *J Atmos. Sci*., **78**, 2895-2909.

528 Davies-Jones, R. P., R. J. Trapp, and H. B. Bluestein, 2001: Tornadoes and tornadic storms.
529 *Meteor. Monogr.*, No. 50, 167–221.

530 Kuo, H. L., 1966: On the dynamics of convective atmospheric vortices. *J. Atmos. Sci.*, **23**, 25-
531 42.

532 Lilly, D. K., 1982: The development and maintenance of rotation in convective storms.
533 *Intense Atmospheric Vortices*, L. Bengtsson and J. Lighthill, Eds., Springer-Verlag, 149–
534 160.

535 Lilly, D. K., 1986: The structure, energetics and propagation of rotating convective storms.
536 Part II: Helicity and storm stabilization. *J Atmos. Sci*., **43**, 126-140.

537 Salmon, R., 1998: *Lectures on Geophysical Fluid Dynamics*. Oxford University Press, 378
538 pp.

539 Scorer, R. S., 1997: *Dynamics of Meteorology and Climate*. Praxis, 686 pp.

540 Shapiro, A. H., 1972: Vorticity. *Illustrated Experiments in Fluid Mechanics: The NCFMF*
541 *Book of Film Notes*. MIT Press, 63-74. Available online at
542 http://web.mit.edu/hml/ncfmf/09VOR.pdf

543 Siebert, P., 1993: Convergence and accuracy of numerical methods for trajectory
544 calculations. *J. Appl. Meteor*., **32**, 558-566.

545